Prediction of Grain Structure Evolution During Rapid Solidification of High Energy Density Beam Induced Re-Melting

T.F. Flint, C. Panwisawas, Y. Sovani, M.C. Smith, H.C. Basoalto

PII: S0264-1275(18)30215-6
DOI: doi:10.1016/j.matdes.2018.03.036
Reference: JMADE 3778

To appear in:

Received date: 28 November 2017
Revised date: 15 January 2018
Accepted date: 14 March 2018

Please cite this article as: T.F. Flint, C. Panwisawas, Y. Sovani, M.C. Smith, H.C. Basoalto, Prediction of Grain Structure Evolution During Rapid Solidification of High Energy Density Beam Induced Re-Melting, (2018), doi:10.1016/j.matdes.2018.03.036

Prediction of Grain Structure Evolution During Rapid Solidification of High Energy Density Beam Induced Re-Melting☆

T.F. Flint[a,*], C. Panwisawas[b,*], Y. Sovani[b], M.C. Smith[a], H.C. Basoalto[b],

[a] *Dalton Nuclear Institute, The University of Manchester, Manchester M13 9PL, UK*
[b] *School of Metallurgy and Materials, The University of Birmingham, Edgbaston, Birmingham B15 2TT, UK*

Abstract

Grain boundary migration in the presence of concentrated sources of heat is a complex process that has a considerable impact on resultant material properties. A phase field model is presented incorporating thermal gradient and curvature driving force terms to predict how a poly-crystalline network evolves due to the application of such heat sources, as grain boundaries migrate due to local boundary curvature and time varying thermal gradients. Various thermal scenarios are investigated, in both two and three dimensions. These scenarios include both partial and full penetration laser induced melting, the application of a linearly varying time-independent thermal field, and successive melting events where regions experience multiple melting and solidification cycles. Comparisons are made between the microstructures predicted by the proposed phase field method, during the various thermal scenarios, that agree with commonly observed phenomena. Particularly interesting is the ability to explain the differences in grain morphology between the full penetration and partial penetration welds using the phase field model and associated driving force magnitudes between the two scenarios. The model predicts the restoration of grain boundary networks in regions experiencing multiple melting events, and explains the differences in grain morphology due to the local curvature and thermal gradient effects.

Keywords: Phase Field, Thermal Field, Re-Melting, Thermal Gradient, Grain Boundary Migration

1. Introduction

Understanding solid-to-liquid transitions in advanced processes such as additive manufacturing and welding is fundamental in establishing causal relation-

*Corresponding author
Email address: Thomas.Flint@manchester.ac.uk (T.F. Flint)

ships between process parameters, emerging alloy microstructures and properties. These are crucial for the development of integrated computational materials engineering (ICME) tools in order to predict location specific material properties. To achieve this aim a multi-scale materials modelling approach to the solidification process is required that explicitly simulates emerging microstructures as a function of spatial and temporal changes of an applied heat source. Due to the extreme conditions found within a high energy density beam, a number of challenges arise in trying to simulate the resulting microstructure. The large spatial variation in the incident energy density associated with these processes results in steep thermal gradients that rapidly evolve. The evolution of the thermal field in a material subjected to such a high energy density source is influenced by the complex flows of the liquid metal, and gives rise to a rich range of potential grain structures (equiaxed and columnar). A number of numerical schemes have been developed over the last few decades for modelling grain nucleation and growth. However, to the best of the author's knowledge, no such computational studies have been reported in the scientific literature focusing on remelting events commonly encountered in additive manufacture or fusion welding.

The migration of grain boundaries is an important phenomenon during the processing of poly-crystalline materials. Grain boundaries migrate in response to driving forces acting upon them in such a manner as to minimise the total free energy in the entire system. Following grain boundary (GB) migration, the resulting microstructure has significant effects on the macro-scale properties of the material. The coarsening of grains and migration of grain boundaries may favourably or adversely affect the properties influenced by a component's microstructure [1]. Mechanical, thermal and electromagnetic properties are all affected by altering the microstructure and grain size distribution. As such, mechanisms governing the microstructural evolution are of great interest both academically and industrially.

There are a number of physical mechanisms reported in the scientific literature that contribute to the driving forces dictating GB evolution [2]. The most relevant sources include stored deformation energy, the GB energy due to the curvature of the boundary, and forces arising from applied external fields. The applied external fields may include a global elastic deformation, or perhaps an applied magnetic field if the material is susceptible. One of the most common externally applied fields is a thermal field. The resulting driving force on the grain boundaries due to a thermal gradient causes the boundary to migrate up the applied energy gradient as atoms traverse from the hotter side of the GB to the colder side [2, 3]. An applied temperature field initiates a thermal gradient, causing migration of the grain boundaries explicitly, as well as increasing the mobility of grain boundaries; hotter grains are more able to migrate subject to other driving forces, such as the curvature driving force.

It has been a primary goal of computational efforts in materials science to develop the capability to model microstructural evolution under realistic conditions with predictive accuracy [4, 5]. Several techniques have emerged for the simulation of grain growth; Monte Carlo (MC) Potts model [6, 7], vertex model

[8], cellular automata [9] and the phase field (PF) method [10, 11] are the most common methods used. Despite significant differences in underlying methodology, the different approaches have been shown to predict similar behaviour in simulations of two dimensional coarsening. The MC method for simulating coarsening of grains has proven popular due to favourable computational costs when compared with the PF approach [6]. Although the computational expense of the PF method is relatively high, due to the need to appropriately resolve the field boundaries, a major advantage of this approach is its scope for incorporation of the applied driving forces on grain boundaries. These forces cannot be readily incorporated into statistical approaches and may lead to the development of complex microstructures. It is now possible to simulate a microstructure using the PF method, such that the simulated volume is statistically significant and representative [12].

In a PF formulation, the boundary energy is introduced through gradient energy terms in the free energy functional similar to the treatment of anti-phase domain boundaries by Allen and Cahn [4, 13]. The main advantage of this model is that continuous tracking of GB position is not required since the locations of grain boundaries are implicitly defined by the regions where the gradients of field variables are non-zero. Also the Gibbs-Thomson effect is naturally incorporated in the governing equation [4, 14, 15]. The PF method, is considered to be the most versatile and mature approach for simulating coarsening phenomena, particularly in the presence of multiple phases or gradients of concentration, stress or temperature [16, 17]. Presented in this work is a constrained multi-phase field model, extended to incorporate the driving force on a GB due to large thermal gradients, such as those present in the high energy density beam welding of metallic alloys [15].

The primary focus of this paper is to present a theoretical and numerical framework to study grain structure evolution during a remelting event. In particular, to derive statistical behaviour from PF modelling of interface motion across complex thermal fields representing fusion welding of a titanium alloy system. A PF scheme is presented in Section 2, which includes thermal gradient contributions to the evolution of the order parameter. In this section, a method to consider isotropic GB behaviour is discussed. Section 3 presents the fluid mechanics model used to simulate the development of a fusion weld representing *Ti-6Al-4V*. Process conditions associated with partial and full penetration welds are simulated, as well as scenarios where the material undergoes numerous melting and solidification cycles. Numerical results and discussion are given in Section 4 corresponding to simulations of the high energy density melting scenarios, as well as the simulation of the microstructural behaviour in a linearly varying thermal field. Finally the conclusions of the work are summarised in Section 5.

2. Phase Field Model

Historically, the form of the free energy in the derivation of the PF evolution equations has been assumed to be isothermal and boundary motion driven

primarily by local curvature. In the presented work, terms are added to the free energy expression to represent the driving force on the grain boundaries due to spatial and temporal variations in the global temperature field. In general the velocity of a migrating boundary, v, is found by taking the product of the GB mobility with the driving pressure acting upon it. The driving pressures acting on the grain boundaries in the presented work are considered to be the curvature driving pressure, F_c, and the thermal gradient driving pressure, F_t. The GB velocity is then given as the superposition of these pressures as

$$v = m\left(F_t + F_c\right) \tag{1}$$

The curvature driving pressure has been investigated in many works and is given by $F_c = -\sigma\kappa$, where m is the GB mobility, κ is the local curvature and σ is the GB energy. [2, 15]. The thermal gradient driving pressure, F_t, has not received the same level of scrutiny. F_t was first stated in the book by Gottstein and Shvindlerman [2] and the derivation provided by Bai et al. [18]. It is trivial to extend the one dimensional temperature field provided by Bai et al. to a three dimensional field [18]. The equation for F_t is then given as

$$F_t = \frac{2\lambda\Delta S}{\Omega}\nabla T \tag{2}$$

where ΔS is the entropy difference between the GB and the crystal which is approximately equal to the melting entropy, 2λ is the GB width, T is the temperature and Ω is the molar volume of the material which may readily be found from the density and molar mass. The validity of the assumptions in the derivation of F_t (that ΔU_i and ΔS_i are temperature-independent) has been investigated using a number of molecular dynamics simulations. It has been found that the proposed theoretical expression for the thermal gradient driving force, shown in Equation 2, is valid [18]. The GB velocity due to the superposition of the local curvature and thermal gradients is then given by

$$v = m\left(\frac{\Delta S 2\lambda}{\Omega}\nabla T - \sigma\kappa\right) \tag{3}$$

m is strongly temperature dependent and is often assumed to follow an Arrhenius-type relationship of the form

$$m = m_o \exp\left(-\frac{Q}{k_B T}\right) \tag{4}$$

where Q is the activation energy for the GB under consideration, m_0 is a pre-exponential constant and k_B is the Boltzmann constant.

In the PF model, boundaries between fields representing grains are considered as diffuse interfaces of a finite width. The orientation, or phase, of the field changes gradually over this boundary. An order parameter, ϕ_n, is utilised to represent the orientation in the model consisting of N grains. In the presented PF model the GB energy and mobility are assumed to be isotropic, so that they do not vary with relative misorientation of the boundaries. Consider a GB

between two regions, $\phi_n = 1$ and $\phi_m = 1$. At the interface between these two fields the magnitude of the ϕ_n and ϕ_m fields varies smoothly in such a manner that the sum of the fields, indeed the sum over all order fields in the domain remains unity [13, 19, 20]

$$\sum_{n=1}^{N} \phi_n = 1 \tag{5}$$

The diffuse interface approach has been chosen for several reasons. The diffuse interface model maintains the force balances at triple junctions. The model also adopts the parabolic potential with a double obstacle, which results in a definite boundary within the PF, preventing diffuse transport of fields into neighbouring grains [4, 21]. A step function is defined to determine the number of co-existing phases as shown in Equation 6. The number of phases co-existing at a given point is then given by Equation 7

$$s_n = \begin{cases} 1; \forall \phi_n > 0 \\ 0; \forall \phi_n = 0 \end{cases} \tag{6}$$

$$S = \sum_{n=1}^{N} s_n \tag{7}$$

In order to determine the evolution of the N-coupled PFs that represent the grains, one must consider the free energy within the system, and the driving forces arising due to this energy. In the presented work the free energy is presented as an integral of the density functional over the domain Ω. The density functional is split into two parts: the GB energy density $f_{GB}(\boldsymbol{x}, t)$; and the thermal energy density $f_T(\boldsymbol{x}, t)$

$$F(t) = \int_{\Omega} \left\{ f_{GB}(\boldsymbol{x}, t) + f_T(\boldsymbol{x}, t) \right\} d^3\boldsymbol{x} \tag{8}$$

The evolution equation for the PF is given by

$$\frac{\partial \phi_q}{\partial t} = \frac{2M_\phi}{S} \sum_{p \neq n}^{N} s_p s_n \left(\frac{\delta F}{\delta \phi_n} - \frac{\delta F}{\delta \phi_p} \right) \tag{9}$$

where M_ϕ is the isotropic PF mobility [4, 15]. The variation in the free energy density due to the GB curvature and thermal gradient driving forces is given by Equation 10

$$\frac{\delta F}{\delta \phi_n} = \sum_{m \neq n}^{N} \left(\frac{\epsilon^2}{2} \nabla^2 \phi_m + \omega \phi_m - \frac{\mu}{2} \nabla \phi_m \cdot \nabla T \right) \tag{10}$$

where ϵ is the gradient energy coefficient, T is the temperature, μ is the temperature gradient energy coefficient, and ω is the height of the parabolic potential with a double obstacle. The final term on the RHS of Equation 10 is naturally proposed for the thermal gradient contribution; this expression will be shown to reproduce the expected behaviour of a boundary in a thermal gradient as the boundary migrates to minimise the total free energy in the system. Removing this term produces the familiar PF expression for the evolution of a boundary network due to curvature driving forces [14, 15]. The parameters ϵ, ω, μ and

M_ϕ have definite relationships with the GB energy, σ, PF boundary width, 2ξ, boundary entropy difference, ΔS, GB width, 2λ, alloy molar volume, Ω, and mobility m of a GB.

2.1. Sharp Interface Limit Analysis

The interface width, 2ξ and GB energy σ, for a boundary between two grains are given by $2\xi = {}^{\pi\epsilon}/_{\sqrt{2\omega}}$ and $\sigma = \frac{\pi}{8}\epsilon\sqrt{2\omega}$ respectively [4, 15]. To determine the relationships between the other PF GB parameters, in order to simulate physical systems, further considerations must be made. Consider a boundary between two fields ϕ_q and ϕ_n, utilising Equation 5, Equation 9 reduces to

$$\dot{\phi_q} = M_\phi \left[\epsilon^2 \nabla^2 \phi_q + \mu \nabla \phi_q \cdot \nabla T + \omega \left(1 - 2\phi_q\right)\right] \tag{11}$$

The PF mobility, M_ϕ, has a relationship with the GB mobility, m. The relationship may be found by considering a shrinking grain in spherical co-ordinates, as first considered by Allen and Cahn [13]. Consider a spherical q field with curvature κ, in a position dependent temperature field. Using a general expression for the divergence of a gradient vector to a scalar field, Equation 11 may be expressed as [22]

$$\frac{1}{M_\phi}\frac{\partial \phi_q}{\partial t} = \frac{v}{M_\phi}\frac{d\phi_q}{dr} = -\epsilon^2 \frac{d^2\phi_q}{dr^2} - \epsilon^2 \kappa \frac{d\phi_q}{dr} + \mu \frac{d\phi_q}{dr}\nabla T + \omega\left(1 - 2\phi_q\right) \tag{12}$$

where v is the field shrinkage velocity, ${}^{dr}/_{dt}$. A sharp interface limit of ${}^{1}/_{\kappa} \gg \xi$ is assumed [13, 15]. Integrating Equation 12 from ${}^{1}/_{\kappa} - \xi$ to ${}^{1}/_{\kappa} + \xi$ yields

$$\left[-\frac{v}{M_\phi}\phi_q\right]_{{}^{1}/_{\kappa}-\xi}^{{}^{1}/_{\kappa}+\xi} = \left[\epsilon^2 \frac{d\phi_q}{dr} + \epsilon^2 \kappa \phi_q - \mu \phi_q \nabla T - \omega r \left(1 - 2\phi_q\right)\right]_{{}^{1}/_{\kappa}-\xi}^{{}^{1}/_{\kappa}+\xi} \tag{13}$$

At the upper bound of the sharp interface limit, ${}^{1}/_{\kappa} + \xi$, the value of the ϕ_q field tends to zero and the value of the gradient of the field variable with respect to r also tends to zero; at the lower bound of the sharp interface limit, ${}^{1}/_{\kappa} - \xi$, the value of ϕ_q tends to unity, the value of ${}^{d\phi_q}/_{dr}$ tends to zero. Inputting the values of the field variable, the gradients of the order parameter and the limits of the integration into Equation 13, it can be shown that

$$-\frac{v}{M_\phi}\left[0 - 1\right] = \epsilon^2 \kappa \left[0 - 1\right] - \mu \nabla T \left[0 - 1\right] \tag{14}$$

Therefore, the GB mobility can be expressed as

$$v = M_\phi \left(\mu \nabla T - \epsilon^2 \kappa\right) \tag{15}$$

Equating this expression for the PF velocity with the expression for the GB velocity, Equation 3

$$M_\phi \left(\mu \nabla T - \epsilon^2 \kappa\right) = m \left(\frac{2\lambda \Delta S}{\Omega} \nabla T - \sigma \kappa\right) \tag{16}$$

Considering the case of a flat boundary, such that the curvature, $\kappa = 0$, all relationships between PF and GB properties may be determined. In this case the expression for μ is

$$\mu = \frac{m}{M_\phi} \frac{2\lambda \Delta S}{\Omega} \tag{17}$$

When the original curved boundary is considered, and this expression is inserted into Equation 16 it is clear that $M_\phi \epsilon^2 \kappa = m\sigma\kappa$. Therefore $M_\phi = {}^{m\sigma}/_{\epsilon^2} = {}^{\pi^2 m}/_{16\xi}$ and after substituting for m/M_ϕ in the expression for μ

$$\mu = \frac{16\xi 2\lambda \Delta S}{\pi^2 \Omega} \tag{18}$$

The above equations describe isotropic grain growth due to the curvature and thermal gradient driving forces. It is worth noting at this point that the expression μ is similar to that found by other authors [3], considering thermal driving forces on grain boundaries but neglecting the adoption of the parabolic potential term, using the alternate PF approach of Moelans *et al.* [23].

3. Computing the Transient Thermal and Phase Field

This work focuses on the simulation of microstructure evolution during melting and remelting events, such as those encountered in fusion welding. The previous section presented an interface framework to simulate solidification. In order to implement the thermal gradient driving force and temperature field into the PF model, a representative thermal field must be computed. This section will give a theoretical outline of the metal solid-liquid transition during fusion welding for predictions of the thermal fields required by the PF model. There are various methods by which an appropriate temperature field, representative of the welding process, may be obtained. One may wish to perform a finite element simulation and treat the domain as a solid body and apply a representative area or volumetric heat flux distribution in motion, solving the heat equation for the desired temperature [24]. Another method would be to obtain the analytical solution for a representative heat source model and therefore remove numerical uncertainties from the calculation procedure [25]. However, such approaches are limited. An alternative is to directly calculate the thermal fields from the dynamics of the liquid metal. This will involve full thermal fluid simulations of a high power laser incident on the surface of a substrate material, fully capturing the solid to liquid state transition as well as the momentum field in the domain and coupled temperature field. Such a framework is implemented in the current work for the computation of the temperature field.

The momentum and other fluid properties of the mixture are formulated as a single momentum equation coupled with equations for energy and continuity.

These are solved to rationalise the evolution of the metallic and gaseous phases. The metallic phase was treated as a single material (metal) with multiple phases (solid, liquid and gas). The standard balance of forces and conservation of momentum and energy is used and the model assumes that the Reynolds number of the molten liquid metal is sufficiently low such that a laminar solver is appropriate. Similar assumptions are made in other computational fluid dynamics (CFD) modelling approaches for fusion welding [26–28]. To simulate the laser interaction with the material, an engineering approximation of a laser volumetric heat source (e.g. [29]) is used to represent the multiple reflections by a volumetric energy density.

A brief summary of the physical phenomena used in simulating the interaction between heat source and material is as follows. The solid, liquid and vapour metal constitutive behaviours are defined within the metallic phase by introducing appropriate phase transformations depending on the temperature, being either below the solidus, between the solidus and liquidus temperature, above the liquidus temperature or above the vaporisation temperature. Above the vaporisation temperature, metal liquid transforms to metal vapour. The latter vapour phase is assumed to be converted into atmospheric gaseous phase. The loss of metallic phase, due to evaporation when the evaporation temperature is reached, is included into the Navier-Stokes (momentum) equation of the liquid metal and metal vapour. It also includes reaction surface forces, in the present treatment, from vaporisation (as a function of the vapour recoil pressure [27, 30–32]), surface tension and Marangoni force. All surface forces act only on the metal liquid/vapour interface. In addition, the buoyancy force term caused by density differences due to thermal expansion and a damping force associated with the frictional dissipation in the mushy zone given by Carman-Kozeny equation which is an enthalpy method for phase changes [33, 34] are used. The thermal energy is coupled with a momentum contribution and balanced between the heat input due to the source term, Q_T, proposed by Xu et al. [29], and the heat loss due to conduction, convection, radiation and evaporation [35, 36].

A volume of fluid approach was adopted for the thermal-fluid calculation; here the sum of metal α_1 and gas α_2 phase fractions is maintained at unity, $\alpha_1+\alpha_2 = 1$. The weight function of any parameter x, defined as $\bar{x} = x_1\alpha_1+x_2\alpha_2$, is used to smear out the effect of metal and gas phases. To rationalise the melt dynamics, fluid flow and heat transfer equations needed to be solved. Starting with the assumption of incompressible fluid the continuity condition on the velocity field $\boldsymbol{u}$ is written as

$$\boldsymbol{\nabla} \cdot \boldsymbol{u} = 0 \tag{19}$$

The computation domain is divided into a metallic α_1 region and atmospheric gaseous α_2 regions. The solid, liquid and vapour metal constitutive behaviours are defined within α_1 by introducing appropriate phase transformations depending on the temperature, being either below the solidus, between the solidus and liquidus temperature, above the liquidus temperature or above the vaporisation temperature. The volume occupied by the α_1 phase will evolve through the

following differential equation,

$$\frac{\partial \alpha_1}{\partial t} + \boldsymbol{\nabla} \cdot (\alpha_1 \boldsymbol{u}) = -\frac{\dot{m}_V}{\rho_2} \tag{20}$$

where t is time, and the sink term in the right hand side (RHS) of Equation 20 describes the loss of metallic phase due to evaporation when the evaporation temperature T_v is reached. In this work, ρ_2 is referred to the density of metal vapour which is equivalent to the atmospheric gas phase as chemical species is not distinguished here. The mass evaporation rate $\dot{m}_v$ is a function of the vapour recoil pressure p_v. The governing field equation describing the flows of the liquid metal in weld pool and metal vapour is the Navier-Stokes equation,

$$\begin{array}{c} \frac{\partial \bar{\rho} \boldsymbol{u}}{\partial t} + \boldsymbol{\nabla} \cdot (\bar{\rho} \boldsymbol{u} \otimes \boldsymbol{u}) = -\boldsymbol{\nabla} p + \boldsymbol{\nabla} \cdot \mathrm{T_v} \\ + f_{buoyancy} + f_{melting} + f_{surface} \end{array} \tag{21}$$

where $\mathrm{T_v}$ is the viscous deviatoric stress tensor, p is the hydrostatic pressure and $\bar{\rho}$ is the density. Three source terms are present on the RHS of Equation 21. The buoyancy force term $\boldsymbol{f}_{buoyancy}$ is caused by density differences due to thermal expansion. The melting source term, $\boldsymbol{f}_{melting}$ damping force associated with the frictional dissipation in the mushy zone given by Carman-Kozeny equation which is an enthalpy method for phase changes [33, 34] are used. A number of mechanisms contribute to the surface force, $\boldsymbol{f}_{surface}$, including normal and tangential components of surface tension; where in the present treatment the tangential component of surface tension arises due to the temperature dependent Marangoni convection effect. The Marangoni force is a thermo-capillary force that arises from temperature gradients across the liquid/gas interface [37–39]. The conservation of thermal energy is given as,

$$\begin{array}{c} \frac{\partial \bar{\rho} \bar{C}_p T}{\partial t} + \boldsymbol{\nabla} \cdot (\bar{\rho} \boldsymbol{u} \bar{C}_p T) = -\frac{\partial \bar{\rho} \Delta H}{\partial t} - \boldsymbol{\nabla} \cdot (\bar{\rho} \boldsymbol{u} \Delta H) \\ + \boldsymbol{\nabla} \cdot (\bar{k} \boldsymbol{\nabla} T) - [Q_V |\boldsymbol{\nabla} \alpha_1| + Q_T] \frac{2 \bar{C}_p \bar{\rho}}{(C_{p1} \rho_1 + C_{p2} \rho_2)} \end{array} \tag{22}$$

where T is the temperature, $\bar{C}_p$ is the specific heat of the metallic phase and H is the latent heat. Equations 20, 21 and 22 are solved to quantify the flow dynamics of the melt. By solving the set of governing equations, the evolution of melt kinetics and liquid/gas interface change can be analysed and rationalised. A detailed model description is to be published elsewhere [40–42] and model parameters were adopted from [43–45].

3.1. Computational Procedures

The thermal fluid flow calculation has been developed using the C++ open source code OpenFOAM (Open Field Operation And Manipulation) toolbox. A solver for two incompressible, non-isothermal immiscible fluids using a volume of fluid phase-fraction based interface capturing approach is adopted from Panwisawas et al. [42]. The phase fields and thermal fields are coupled by a staggered time integration procedure. For any given time-step, Equations 20, 21 and 22 are solved using a volume-of-fluid approach to capture the temporal and

spatial evolution of liquid metal/gas interface to capture the transient physical effects during the heat source-material interaction of a fusion welding process. The weighted average is used to take into account two immiscible fluids as one effective fluid throughout the calculation domain. The model makes use of the two-fluid Eulerian model for two-phase flow, where phase fraction equations are solved separately for each individual phase. The physical properties are calculated based on the distribution of the liquid volume fraction, and thus they are equal to the properties of each fluid in their corresponding occupied regions and varied only across the interface. In this model, a sharper interface resolution is considered through an additional convective term originating from modelling the velocity in terms of weighted average of the corresponding liquid and gas velocities is introduced into the transport equation for phase fraction. To allow sharp interface resolution, numerical diffusion, which is unavoidably introduced through the discretisation of convective terms, can be controlled and minimised through the discretisation of the compression term. In order to ensure stability of the solution procedure, the calculations are performed using a self-adapting time step which is adjusted at the beginning of the time iteration loop based on the Courant number. Moreover, in order to achieve a proper coupling between velocity and pressure it is necessary to adapt the PISO (Pressure Implicit with Splitting of Operators) loop to the momentum equation and derive a new pressure equation for each time step. The three dimensional temperature field is then passed to the PF calculation portion of the code where the spatial gradients of the temperature field are calculated. The evolution of the PF variables is then calculated by solving Equation 9 over the entire domain, and all order parameters, using the forward Euler method to update the PF variables, ϕ.

Once a point in the computational domain exceeds the solidus temperature of the *Ti-6Al-4V* system under consideration, the PF variable, ϕ, at this location is assigned a random orientation. This randomisation of the PF variable in the molten regions of the system is performed at every time-step in the simulation until the region solidifies once again and ensures that no grain structure is permitted to develop in the melt.

The effect of the GB width, 2ξ, on the accuracy of the PF simulation was investigated, as will be discussed in Sub-section 4.1, and it was determined that increasing the number of cells in the boundary region leads to improved accuracy of the simulation accuracy. There is however a trade-off between accuracy and computation time. In the simulations of grain-boundary networks in this work the PF boundaries were permitted to span a minimum of 10 cells. This appeared to be a reasonable compromise between the solution accuracy and computational efficiency of the PF simulation.

4. Results and Discussion

Whilst direct microstructural comparisons are not made in the presented work; a number of scenarios are investigated and the effect of parameter alterations are investigated and commented on in the resulting predicted microstructure. All simulations in the current work are representative of *Ti-6Al-4V*. Mate-

rial and model parameters associated with the CFD have been determined from previous work [42]. The parameters for the PF simulation are shown in Table 1 The molar volume of *Ti-6Al-4V* is calculated from the density and molar mass. The relative entropy difference between the boundaries and bulk in the domain, ΔS, is estimated from the melting enthalpy. The pre-exponential factor, m_0, present in Equation 4 for the *Ti-6Al-4V* system is not known and there is very little information of this parameter for engineering alloy systems. However, pure aluminium alloy systems have been investigated and therefore the value of this parameter is taken from this work [46]. It is worth noting that the simulations were far more sensitive to the activation energy, Q, than the pre-exponential factor, m_0, and so this is a reasonable assumption.

Table 1: Parameters used in the PF simulation of *Ti-6Al-4V* microstructures.

Parameter	*Ti-6Al-4V*
$\sigma\ \left(kg\,s^{-2}\right)$[47]	0.81
$\Omega\ \left(mm^3\,mol^{-1}\right)$	100.3×10^3
$\Delta S\ \left(kg\,mm^2\,s^{-2}\,K^{-1}\,mol^{-1}\right)$	152.9×10^6
$T_s\ (K)$	1878.0
$Q\ (eV)$[48]	1.0
$2\lambda\ (nm)$	5.0
$m_0\ \left(mm^2\,s\,kg^{-1}\right)$[46]	178.0

The parameters in Table 1 are not trivial to determine. Certain parameters have a greater effect on the GB motion in the temperature field and therefore the resultant distribution in grain sizes. The activation energy, Q, has a drastic effect on the mobility of the grain boundaries in the simulation. It is therefore crucial to have a representative value for this parameter corresponding to the material being simulated. For a given time varying thermal field; a higher Q will tend to reduce the GB mobility over the network while a lower Q will increase the network mobility. Therefore if the activation energy value inserted into the PF simulation is too low compared with the physical value for the given material, the PF simulation would over-predict the amount of coarsening occurring in the region under consideration and the grain size distributions would be shifted towards a larger grain size. As shown in Equation 3 the GB width, 2λ, entropy difference, ΔS, and molar volume, Ω, have a direct influence on the migration velocity in the PF model. Inserting a value for 2λ into the PF computation that is too low with respect to the physical value will dampen the velocities of the boundaries over the temperature range and effectively reduce the amount of coarsening occurring in the simulation. A value for ΔS that is erroneously low will have a similar effect while a low value for Ω will have the opposite effect as this term appears in the denominator rather than the numerator for the driving force expression.

4.1. Investigating a Single Grain Boundary present in a Linear Thermal Field

In order to investigate the effect of the thermal gradient driving force, a single GB was considered. A 2D domain, $20\,\mu m$ wide and $10\,\mu m$ high, was seeded with two grains; the domain contained $500,000$ calculation points, in a grid of 1000×500. Figure 1a shows how a boundary in a thermal gradient of $18.9 \times 10^6\,Km^{-1}$ migrates over $2.03\,\mu s$.

Figure 1b shows the location of a PF boundary, with a width of $400\,nm$, as a function of for various thermal gradients. The mobility of the boundary was arbitrarily set to $m = 1$ for this investigation.

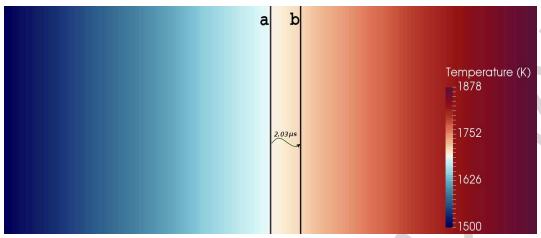

(a) Initial position, (a), and position at $2.03\,\mu s$, (b), for a boundary in a thermal gradient of $18.9 \times 10^6\,Km^{-1}$.

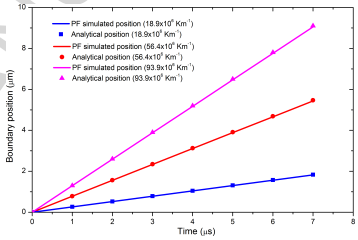

(b) PF boundary location as a function of time for various thermal gradients.

Figure 1: Behaviour of a single boundary, with $\kappa = 0$, in various thermal gradient magnitudes, and the effect that these gradients have on the migration velocity.

The agreement between the phase field boundary location, and the analytically predicted boundary location found by integrating Equation 3 is extremely good and provides confidence in the presented phase field model.

4.2. Grain Boundary Network Migration in a Linear Thermal Field

The evolution of a GB network in a constant thermal gradient was investigated; in order to ascertain the differences in morphology of the resultant microstructure due to the curvature driving force alone as well as the combined curvature and thermal gradient driving forces. In this simulation the mobility of the grain boundaries followed the Arrhenius-type mobility relationship described in Equation 4. 3200 grains in a thermal gradient of $1.58 \times 10^6\,Km^{-1}$ were seeded in a domain of $1\,mm \times 1\,mm$; the right side of the domain was maintained at the solidus temperature of the alloy, with the opposite side at $300\,K$. The initial grain distribution is achieved using a Voronoi tessellation, which is shown in Figure 2 *(a)*. The evolution of the GB network is then shown, neglecting the thermal gradient driving force, in Figures 2 *(b), (c) and (d). In* Figures 2 *(e), (f) and (g)* both the thermal gradient and boundary curvature driving forces are present.

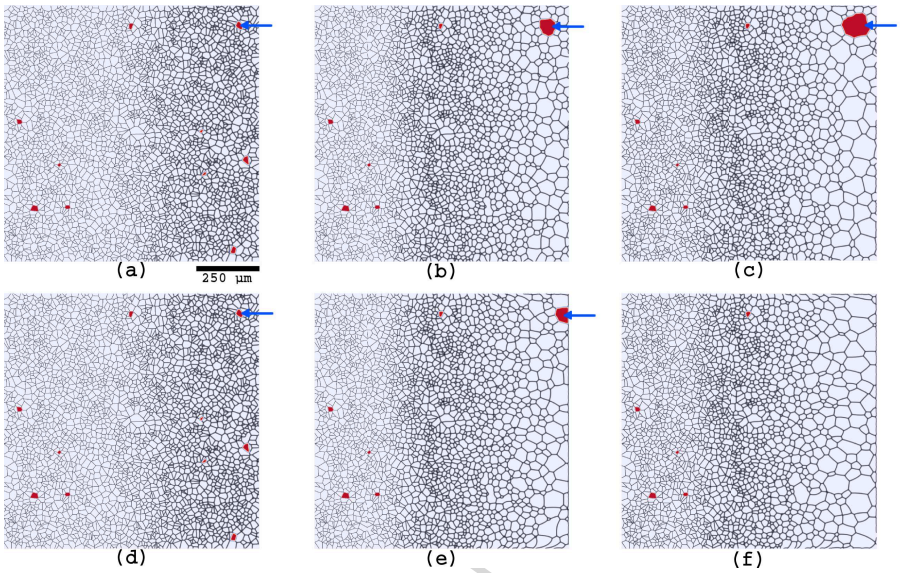

Figure 2: GB network evolution due to curvature driving forces (a, *b* and c) and due to the combined effect of curvature and thermal gradient driving forces (d, *e* and f) from an identical initial grain distribution in a linearly varying temperature field. *(a)* and *(d)* correspond to a time of $0.12 \times 10^{-3}\ s$, *(b)* and *(e)* to $4.92 \times 10^{-3}\ s$, and *(c)* and *(f)* to $9.84 \times 10^{-3}\ s$. Certain grains are highlighted for discussion

As can be seen from Figure 2, only the grains located in regions where the Arrhenius-type mobility is sufficiently high, i.e. where the temperature is sufficiently high, for boundary migration to occur have undergone any grain coarsening. The grains highlighted in red in Figure 2 in the left-half of their respective domains, for both the curvature and combined driving force cases, have experienced little to no coarsening. The effect of the thermal gradient driving force can be clearly seen in Figures 2 *(d), (e) and (f)*; the thermal gradient driving force has caused grains in the hotter region of the domain to preferentially migrate up the thermal gradient. The grain highlighted in red and pointed to by the blue arrow experiences coarsening due to the curvature driving force in both cases. However, with the additional thermal gradient driving force the grain has also preferentially migrated up the thermal gradient to the point where it no longer exists inside the computational domain in Figure 2 *(f)*. The net effect of the additional thermal gradient driving force is to shift the grain size distribution towards the larger grain sizes, this is due to grains migrating to the hot side of the domain and being consumed as their coldest grain boundaries continue to migrate up the thermal gradient in order to minimise the total free energy in the entire system. The domain size does not change, so as there are fewer grains on average, their average size must naturally increase.

The imposed thermal gradient of $1.58 \times 10^{6}\ Km^{-1}$ is of the magnitude one may expect the substrate to experience in high energy density beam welding applications. In these applications the material will exist in solid, fluid and

vapour states over distances of a few *mm*. While the effect of the curvature driving force in the simulation is dominant, it is clear that the thermal gradient driving force should not be omitted when considering GB network evolution in the presence of steep thermal gradients.

4.3. Grain Boundary Migration in a High Energy Density Thermal Field

A temperature field, the generation of which is described in Section 3, is used to simulate the evolution of a GB network subject to the application of a high power density welding heat source. The applied heat source density, Q_T, causes a solid to fluid state change within the metallic region of the computational domain, an example of this can be seen in Figures 3 and 4. The region of the computational domain containing the gaseous phase is omitted from the figures in this section for clarity. However, for completeness it should be noted that the metallic region of the domain was surrounded by gaseous regions above and below the metallic regions shown. As molten regions of the domain cool below the solidus temperature at the solid-liquid boundary, and ϕ is no longer randomised, their curvature is relatively high and so these fields tend to shrink. Existing fields neighbouring these newly precipitated fields which tend to have lower curvature in the solid region tend to grow. In the case where the temperature decreases rapidly following solidification, there may be insufficient time for the boundaries to migrate, as the mobility is a strong function of temperature, and so in this case a series of fields with a high curvature may remain. In any case the fields tend to migrate up the thermal gradient due to the additional thermal gradient free energy driving force. Various temperature fields will be analysed and the differences in the resulting microstructures described in terms of the PF model.

4.3.1. Partial Penetration Melting

In this case the energy density from the laser source is insufficient to generate a melt-pool throughout the thickness of the domain. Figure 3 shows the time evolution of the temperature and $|\phi|$ fields inside the metallic region of the computational domain, representative of *Ti-6Al-4V* grains, as the melt-pool traverses the region. The two dimensional evolution of the GB network, considering isotropic GB behaviour, is shown in Figure 4 at four sequential time steps.

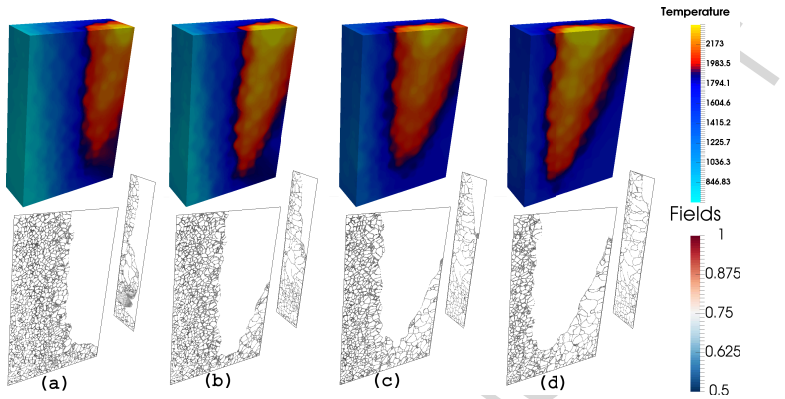

Figure 3: Three dimensional PF simulation of the microstructural evolution around a partial penetration melt-pool in *Ti-6Al-4V*. The thermal and PF magnitudes are shown for four sequential time instances;(a) t=1.25 *ms*: (b) t=3.46 *ms*: (c) t=6.92 *ms*: (d) t=9.44 *ms*.

In the vicinity of the melt pool, the temperature is sufficiently high to increase the mobility of the grain boundaries and enable migration due to their relative curvature and local thermal gradients. The three-dimensional simulations produce fields corresponding to grains of similar morphology to the two-dimensional simulations which are shown in Figure 4.

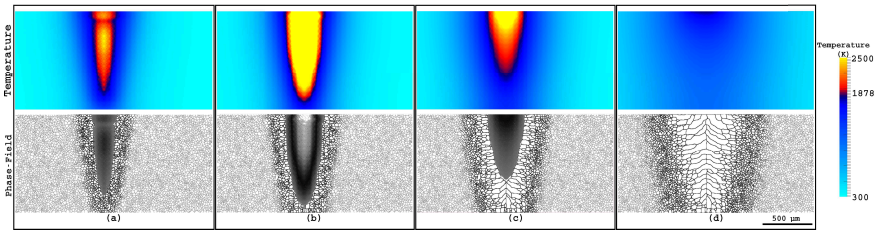

Figure 4: Two dimensional PF simulation of the microstructural evolution around a partial penetration melt-pool in *Ti-6Al-4V* as the domain cools and the material solidifies. The thermal and PF magnitudes are shown for four sequential time instances; (a) t=1.09 *ms*: (b) t=2.19 *ms*: (c) t=6.67 *ms*: (d) t=13.23 *ms*.

Figure 5 shows the grain size distributions for the partial penetration weld. The equivalent diameter is calculated by idealising the irregular grains as circles or spheres.

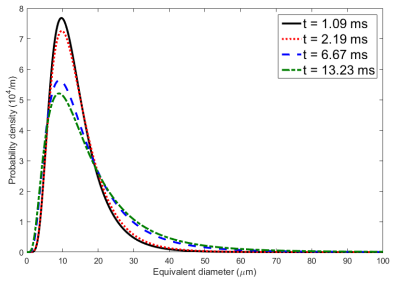

Figure 5: Probability density functions for the GB evolution in a partial penetration weld.

As can be seen in Figures 4 and 5, the effect of the thermal cycle on the GB network is to drastically reduce the number of grains in the domain. As molten region of the domain shrinks and the newly solidified grains are consumed, due to the high local thermal gradients in the region of the solidification front and the large curvature of these new fields, columnar grains grow perpendicular to the solidification front. Following solidification the temperature is sufficiently high for coarsening to proceed for a considerable time. The cooling rate of the domain is low enough that any equiaxed grains that develop in the central region of the domain tend to have sufficient time to be consumed by the incident columnar grains.

4.3.2. Full Penetration Melting

In this case the energy density from the laser source is sufficient to extend the melt-pool through the entire thickness of the substrate material; This is referred to as a full penetration weld. The cooling rate of the molten metallic region is higher for the full penetration case as there are two regions where the metallic fluid was in contact with the gaseous region, the upper and lower surfaces, as opposed to the single region in the partial penetration case where only the upper surface has metallic fluid exposed to the gaseous region. Convection and radiation occur at these locations, with a high temperature gradient at the interface, causing the full penetration domain to cool at a higher rate and therefore the solidification front proceeds at a higher velocity than in the partial penetration case. The drastically higher heat input means that the entire domain still takes longer to solidify, regardless of this higher cooling rate. The thermal field in the metallic region and phase-fields for this full penetration case are shown for four sequential time-steps in Figure 6.

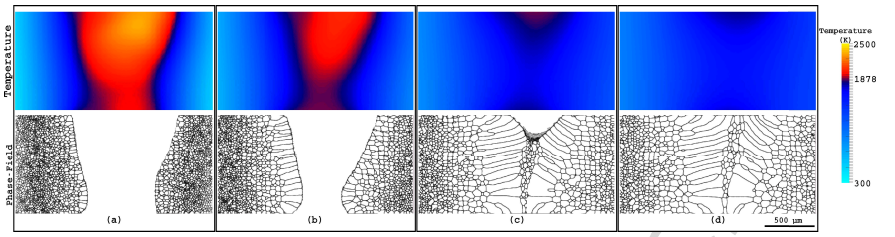

Figure 6: Two dimensional PF simulation, considering misorientation independent GB properties, of the microstructural evolution around a full penetration melt-pool in *Ti-6Al-4V*. The thermal and PF magnitudes are shown for four sequential time instances; (a) t=0.54 *ms* : (b) t=3.21 *ms* : (c) t=6.43 *ms* : (d) t=9.64 *ms* .

As expected the resultant microstructures vary between the partial and full penetration melt-pool cases. As the cooling rate in the metallic region is higher than that of the partial penetration case, there is insufficient time for the small fields that are precipitated out of the melt to be fully consumed by the grains of lower curvature neighbouring them. The result of this is seen by observing the central regions of Figures 4*(d)* and 6*(d)*. The length of the columnar grains extending through the region that was the melt-pool in Figure 6 is greater than those present in Figure 4 as a greater volume of substrate has been melted. This has the additional effect of increasing the average curvature of the columnar grains at the melt interface relative to those present in the partial case, therefore in the full penetration case the disparity between the precipitated fields and the columnar grains that neighbour them is not so large as in the partial penetration case and so the magnitude of the curvature driving force between the columnar grains and precipitated fields is smaller for this case. The result of these effects is the production of equiaxed grains in the central region of the domain where the columnar grains terminate. These equiaxed grains are able to coarsen slightly following solidification as the temperature remains relatively high for a short time. Figure 7 shows the grain size distributions for this case.

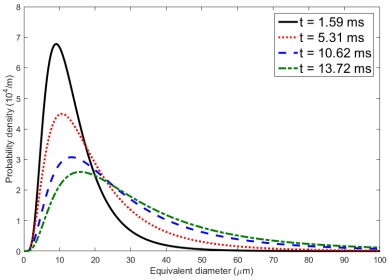

Figure 7: Probability density functions for the GB evolution in a full penetration weld.

As the heat input is higher, a greater area of the domain has experienced melting and coarsening, and as such, the grain size distribution shown in Figure 7 is shifted much further towards the larger grain sizes than Figure 5.

4.3.3. Successive Re-Melting Events

In this case a thermal history representing multiple melting and solidification events was applied to observe the effect on the predicted microstructure. Figure 8 shows the evolution of the predicted microstructure during the second re-melting event where the initial microstructure is that of Figure 4 *(d)*.

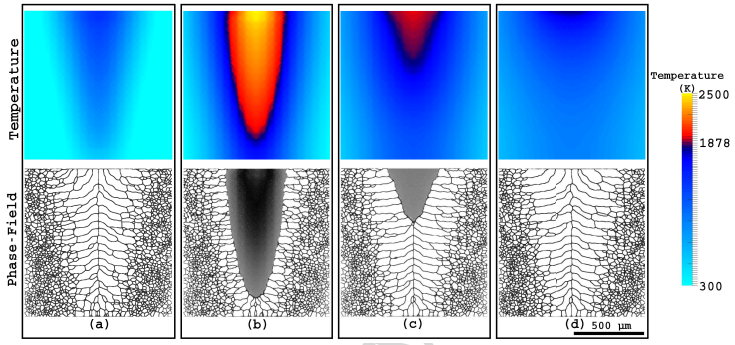

Figure 8: Two dimensional PF simulation, considering misorientation independent GB properties, of the microstructural evolution around a full penetration melt-pool in *Ti-6Al-4V*. The thermal and PF magnitudes are shown for four sequential time instances; (a) t=0 *ms* : (b) t=2.73 *ms* : (c) t=6.56 *ms* : (d) t=12.57 *ms* .

The effect of the dual thermal cycle is clearly visible when comparing the predicted microstructures following a single and double thermal cycle as shown in Figures 8*(a)* and 8*(d)* respectively. The columnar grains extending from the heat affected zone into the fusion zone are longer following a second melting event, although the general morphology of the network is not drastically different between Figures 8*(a)* and *(d)*. This appears to show a degree of GB network restoration following the re-melting event. Figure 9 shows the grain distribution following one, two and three melting events. The corresponding grain size probability density function plots are shown in Figure 10. Note that the shift in the distribution from one to two melting events, is much larger than the shift from two to three melting events, reinforcing the observation that the GB morphology is largely restored following a re-melting event.

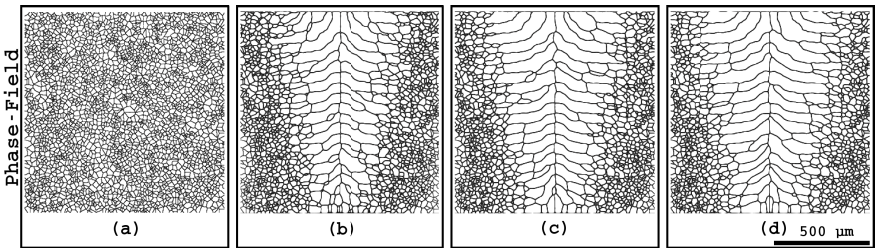

Figure 9: PF simulation of three successive re-melting events showing the initial grain distribution, (a), and the grain distribution after one, (b), two, (c), and three, (d), melting events respectively.

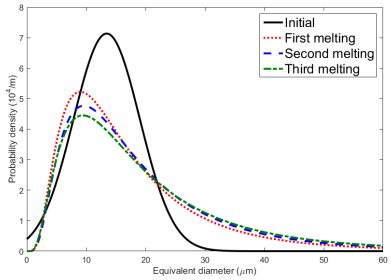

Figure 10: Predicted grain size distributions following successive re-melting events.

It can be seen that the effect of the re-melting events on the grain size distribution decreases as the number of events increases. One may imagine that as the number of re-melting events increases beyond those shown in Figure 10, the change in the grain size distribution will tend to zero for this partial penetration case.

The coupling of the thermal-fluid and PF computations by means of the staggered time integration procedure means that the influence of the variation of phase fields on the thermal fields has not been considered. This method of coupling naturally neglects thermal contributions from the migration of the grain boundaries. However, these migratory thermal contributions in the simulation are negligible when compared with the heat input from the laser heat source and the latent heat contributions from the two state changes of melting and vaporisation considered in the work. Should the heat contribution from the migration of the phase fields have been considered, one would not expect the simulation results to deviate considerably from those reported.

The proposed PF method, incorporating thermal fields that accurately capture the physical processes involved with state change, will provide a more robust understanding of the effect that processing routes have on materials within an ICME framework. Ultimately the proposed method could be employed to determine the ideal physical properties required in a material in order to produce a given coarsening behaviour; this may then be used as a blueprint for the synthesis of these materials.

5. Conclusions

In summary, a modelling approach for the prediction of grain growth and coarsening during high energy density heat source induced melting is presented. The method incorporates both curvature and thermal gradient driving forces into the free energy functional of the PF method. The temperature field generated by a high energy density heat source was calculated from thermal fluid dynamics simulations representative of fusion welding and used to simulate GB network evolution due to such processes in *Ti-6Al-4V*. Specific conclusions can be drawn as follow:

- In large thermal gradients the thermal gradient driving force is significant in promoting the migration of grain boundaries.
- The model provides better understanding of solid-liquid transitions and solid state boundary evolution during fusion and vaporisation state change processes, i.e. fusion welding and powder-bed fusion additive manufacturing.
- The phase field simulation indicates that, with sufficient energy, grain boundaries may migrate up the thermal gradient at a rate equal to the solidification interface velocity.
- A mechanism for the genesis of equiaxed grains at the termination of the columnar grains with high local boundary curvature is proposed and discussed.
- During re-melting events, the proposed model predicts that the grain morphology is statistically restored.

6. Acknowledgements

The work presented in this manuscript is supported by the Engineering and Physical Sciences Research Council (EPSRC) under the "A whole-life approach to the development of high integrity welding technologies for Generation IV fast reactors" grant EP/L015013/1 and the "An Integrated computational materials engineering (ICME) approach to multiscale modelling of the fabrication and joining of powder processed parts" grant EP/P005284/1. The authors would like to thank Trevor Keller and the The Mesoscale Microstructure Simulation Project for for valuable discussions. The raw/processed data required to reproduce these findings cannot be shared at this time as the data also forms part of an ongoing study.

References

[1] M Michiuchi, H Kokawa, Z J Wang, Y S Sato, and K Sakai. Twin-induced grain boundary engineering for 316 austenitic stainless steel. *Acta materialia*, 54(19):5179–5184, 2006.

[2] Gunter Gottstein and Lasar S Shvindlerman. *Grain boundary migration in metals: thermodynamics, kinetics, applications*. CRC press, 2009.

[3] Michael R Tonks, Yongfeng Zhang, Xianming Bai, and Paul C Millett. Demonstrating the Temperature Gradient Impact on Grain Growth in UO2 Using the Phase Field Method. *Materials Research Letters*, 2(1):23–28, 2014.

[4] I Steinbach and F Pezzolla. A generalized field method for multiphase transformations using interface fields. *Physica D: Nonlinear Phenomena*, 134(4):385–393, 1999.

[5] James A Warren, Ryo Kobayashi, Alexander E Lobkovsky, and W Craig Carter. Extending phase field models of solidification to polycrystalline materials. *Acta Materialia*, 51(20):6035–6058, 2003.

[6] H L Wei, J W Elmer, and T DebRoy. Three-dimensional modeling of grain structure evolution during welding of an aluminum alloy. *Acta Materialia*, 2017.

[7] Dana Zöllner and Paulo Rangel Rios. Topological changes in coarsening networks. *Acta Materialia*, 130:147–154, 2017.

[8] Christian Mießen, Nikola Velinov, Günter Gottstein, and Luis A Barrales-Mora. A highly efficient 3D level-set grain growth algorithm tailored for ccNUMA architecture. *arXiv preprint arXiv:1701.06658*, 2017.

[9] Omar Lopez-Botello, Uriel Martinez-Hernandez, José Ramírez, Christophe Pinna, and Kamran Mumtaz. Two-dimensional simulation of grain structure growth within selective laser melted AA-2024. *Materials {&} Design*, 113:369–376, 2017.

[10] Bálint Korbuly, Tamás Pusztai, Gyula I Tóth, Hervé Henry, Mathis Plapp, and László Gránásy. Orientation-field models for polycrystalline solidification: Grain coarsening and complex growth forms. *Journal of Crystal Growth*, 457:32–37, 2017.

[11] Hamed Ravash, Liesbeth Vanherpe, Jef Vleugels, and Nele Moelans. Three-dimensional phase-field study of grain coarsening and grain shape accommodation in the final stage of liquid-phase sintering. *Journal of the European Ceramic Society*, 37(5):2265–2275, 2017.

[12] Eisuke Miyoshi, Tomohiro Takaki, Munekazu Ohno, Yasushi Shibuta, Shinji Sakane, Takashi Shimokawabe, and Takayuki Aoki. Ultra-large-scale phase-field simulation study of ideal grain growth. *npj Computational Materials*, 3(1):25, 2017.

[13] Samuel M Allen and John W Cahn. A microscopic theory for antiphase boundary motion and its application to antiphase domain coarsening. *Acta Metallurgica*, 27(6):1085–1095, 1979.

[14] I Steinbach and M Apel. Multi phase field model for solid state transformation with elastic strain. *Physica D: Nonlinear Phenomena*, 217(2):153–160, 2006.

[15] Seong Gyoon Kim, Dong Ik Kim, Won Tae Kim, and Yong Bum Park. Computer simulations of two-dimensional and three-dimensional ideal grain growth. *Physical Review E - Statistical, Nonlinear, and Soft Matter Physics*, 74(6):1–14, 2006.

[16] V Tikare, E.a. Holm, D Fan, and L.-Q. Chen. Comparison of phase-field and Potts models for coarsening processes. *Acta Materialia*, 47(1):363–371, 1998.

[17] Yoshihiro Suwa, Yoshiyuki Saito, and Hidehiro Onodera. Three-dimensional phase field simulation of the effect of anisotropy in grain-boundary mobility on growth kinetics and morphology of grain structure. *Computational Materials Science*, 40(1):40–50, 2007.

[18] Xian-Ming Bai, Yongfeng Zhang, and Michael R. Tonks. Testing thermal gradient driving force for grain boundary migration using molecular dynamics simulations. *Acta Materialia*, 85:95–106, 2015.

[19] S G Kim, W T Kim, and T Suzuki. Phase-field model for binary alloys. *Physical review. E, Statistical physics, plasmas, fluids, and related interdisciplinary topics*, 60(6 Pt B):7186–7197, 1999.

[20] Gyula I Tóth, Tamás Pusztai, and László Gránásy. Consistent multiphase-field theory for interface driven multidomain dynamics. *Physical Review B - Condensed Matter and Materials Physics*, 92(18):1–19, 2015.

[21] Seong Gyoon Kim, Won Tae Kim, Toshio Suzuki, and Machiko Ode. Phase-field modeling of eutectic solidification. *Journal of Crystal Growth*, 261(1):135–158, 2004.

[22] George Arfken. *Mathematical Methods for Physicists*, volume 40. 1972.

[23] Nele Moelans, Frank Wendler, and Britta Nestler. Comparative study of two phase-field models for grain growth. *Computational Materials Science*, 46(2):479–490, 2009.

[24] T.F. Flint, J.A. Francis, M.C. Smith, and J. Balakrishnan. Extension of the double-ellipsoidal heat source model to narrow-groove and keyhole weld configurations. *Journal of Materials Processing Technology*, 246:123–135, 2017.

[25] T.F. Flint, J.A. Francis, M.C. Smith, and Vasileiou A.N. Semi-analytical solutions for the transient temperature fields induced by a moving heat source in an orthogonal domain. *International Journal of Thermal Sciences*, 123:140–150, jan 2018.

[26] W Tan, N S Bailey, and Y C Shin. Investigation of keyhole plume and molten pool based on a three-dimensional dynamic model with sharp interface formulation. *J. Phys D: Appl Phys.*, 46:55501, 2013.

[27] M Courtois, M Carin, P L Masson, S Gaied, and M Balabane. A new approach to compute multi{{}-{}}reflections of laser beam in a keyhole for heat transfer and fluid flow modelling in laser welding. *J. Phys D: Appl Phys.*, 46:505305, 2013.

[28] Chinnapat Panwisawas, Yogesh Sovani, Richard P Turner, Jeffery W Brooks, Hector C Basoalto, and Isabelle Choquet. Modelling of thermal fluid dynamics for fusion welding. *Journal of Materials Processing Technology*, pages –, 2017.

[29] G X Xu, C S Wu, G L Qin, X Y Wang, and S Y Lin. Adaptive volumetric heat source models for laser beam and laser {{}+{}} pulsed {{}GMAW{}} hybrid welding processes. *Int. J. Adv. Manuf. Technol.*, 57:245–255, 2011.

[30] M Geiger, K.-H. Leitz, H Kock, and A Otto. A 3D transient model of keyhole and melt pool dynamics in laser beam welding applied to the joining of zinc coated sheets. *Prod. Eng. Res. Devel*, 3:127–136, 2009.

[31] X Jin, L Li, and Y Zhang. A study on fresnel absorption and reflections in the keyhole in deep penetration laser welding. *J. Phys D: Appl Phys.*, 35:2304–2310, 2002.

[32] X Jin, P Berger, and T Graf. Multiple reflections and Fresnel absorption in an actual 3{{}D{}} keyhole during deep penetration laser welding. *J. Phys D: Appl Phys.*, 39:4712–4730, 2006.

[33] V R Voller, M Cross, and N C Markatos. An enthalpy method for convection{/}diffusion phase change. *Internaltional Journal for Numerical Methods in Engineering*, 24:271–284, 1987.

[34] F Rösler and D Brüggemann. Shell-and-tube type latent heat thermal energy storage: numerical analysis and comparison with experiments. *Heat Mass Transfer*, 47:1027–1033, 2011.

[35] Y Sun and C Beckermann. Diffuse interface modelling of two-phase flows based nn averaging: mass and momentum equations. *Physica D*, 198:281–308, 2004.

[36] J U Brackbill, D B Kothe, and C Zemach. A continuum Method for Modeling Surface Tension. *Journal of Computational Physics*, 100:335–354, 1992.

[37] L E Scriven and C V Sternling. The Marangoni effects. *Nature*, 187:186–188, 1960.

[38] T Ytrehus and S Ostmo. Kinetic theory approach to interphase processes. *Int. J. Multiphase Flow*, 22:133–155, 1996.

[39] H Ki, P S Mohanty, and J Mazumder. Modelling of high-density laser-material interaction using fast level set method. *J. Phys D: Appl Phys.*, 34:364–372, 2001.

[40] C L Qiu, C Panwisawas, R M Ward, H C Basoalto, J W Brooks, and M M Attallah. On the role of melt flow into the surface structure and porosity development during selective laser melting. *Acta Mater.*, 96:72–79, 2015.

[41] C Panwisawas, C L Qiu, Y Sovani, J W Brooks, M M Attallah, and H C Basoalto. On the role of thermal fluid dynamics into the evolution of porosity during selective laser melting. *Scr. Mater.*, 105:14–17, 2015.

[42] C Panwisawas, C Qiu, M J Anderson, Y Sovani, R P Turner, M M Attallah, J W Brooks, and H C Basoalto. Mesoscale modelling of selective laser melting: Thermal fluid dynamics and microstructural evolution. *Com. Mater. Sci.*, 126:479–490, 2017.

[43] R Rai, J W Elmer, T A Palmern, and T DebRoy. Heat transfer and fluid flow during keyhole mode laser welding of tantalum, {Ti-6Al-4V}, 304{L} stainless steel and vanadium. *J. Phys D: Appl Phys.*, 40:5753–5766, 2007.

[44] R Rai, P Burgardt, J O Mileewski, T J Lienert, and T DebRoy. Heat transfer and fluid flow during electron beam welding of {21Cr-6Ni-9Mn} steel and {Ti-6Al-4V} alloy. *J. Phys D: Appl Phys.*, 42:025503(12pp), 2009.

[45] J Z Li, W L Johnson, and W K Rhim. Thermal expansion of liquid {Ti-6Al-4V} measured by electrostatic levitation. *Appl. Phys. Lett.*, 89:111913, 2006.

[46] Y Huang and F J Humphreys. Measurements of grain boundary mobility during recrystallization of a single-phase aluminium alloy. *Acta Materialia*, 47(7):2259–2268, 1999.

[47] T A Roth and P Suppayak. The surface and grain boundary free energies of pure titanium and the titanium alloy Ti6Al4V. *Materials Science and Engineering*, 35(2):187–196, 1978.

[48] F X Gil, D Rodriguez, and J A Planell. Grain growth kinetics of pure titanium. 33:1361–1366, 1995.

Graphical abstract

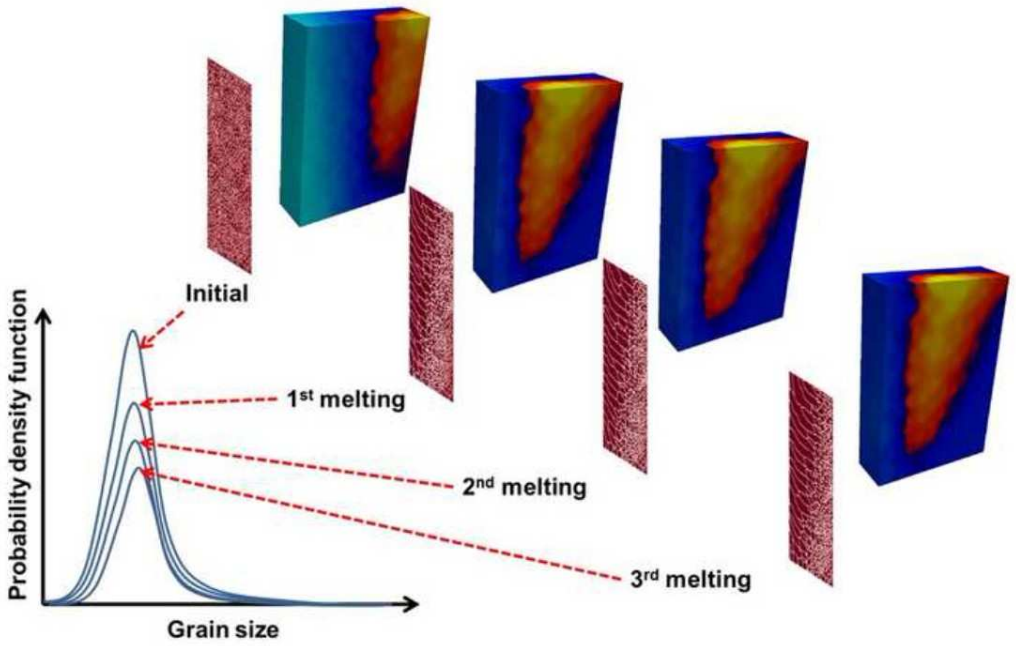

Highlights

- A phase-field formulation considering both boundary curvature and thermal gradient driving forces is presented
- The model is validated against analytically predicted boundary positions for a straight boundary in a linearly varying thermal field
- The model is coupled with a thermal-fluid solution for the prediction of temperature fields and their spatial gradients
- The proposed solution approach is applied to partial penetration and full penetration laser welds, as well as scenarios where the substrate is repeatedly melted and re-solidified
- It is determined that incorporating thermal gradient driving force into the phase-field model is crucial for the accurate prediction of grain boundary evolution which will inform the future design of materials